Monthly Notices
of the
ROYAL ASTRONOMICAL SOCIETY

Mon. Not. R. Astron. Soc. **416,** 2108–2122 (2011) doi:10.1111/j.1365-2966.2011.19182.x

Thermal emission at 4.5 and 8 μm of WASP-17b, an extremely large planet in a slightly eccentric orbit

D. R. Anderson,[1⋆] A. M. S. Smith,[1] A. A. Lanotte,[2] T. S. Barman,[3] A. Collier Cameron,[4] C. J. Campo,[5] M. Gillon,[2] J. Harrington,[5] C. Hellier,[1] P. F. L. Maxted,[1] D. Queloz,[6] A. H. M. J. Triaud[6] and P. J. Wheatley[7]

[1]*Astrophysics Group, Keele University, Staffordshire ST5 5BG*
[2]*Institut d'Astrophysique et de Géophysique, Université de Liège, Allée du 6 Août 17, Bat. B5C, Liège 1, Belgium*
[3]*Lowell Observatory, 1400 West Mars Hill Road, Flagstaff, AZ 86001, USA*
[4]*SUPA, School of Physics and Astronomy, University of St Andrews, North Haugh, St Andrews, Fife KY16 9SS*
[5]*Planetary Sciences Group, Department of Physics, University of Central Florida, Orlando, FL 32816-2385, USA*
[6]*Observatoire de Genève, Université de Genève, 51 Chemin des Maillettes, 1290 Sauverny, Switzerland*
[7]*Department of Physics, University of Warwick, Coventry CV4 7AL*

Accepted 2011 June 3. Received 2011 June 3; in original form 2011 January 30

ABSTRACT

We report the detection of thermal emission at 4.5 and 8 μm from the planet WASP-17b. We used *Spitzer* to measure the system brightness at each wavelength during two occultations of the planet by its host star. By combining the resulting light curves with existing transit light curves and radial-velocity measurements in a simultaneous analysis, we find the radius of WASP-17b to be $2.0R_{\rm Jup}$, which is $0.2R_{\rm Jup}$ larger than any other known planet and $0.7R_{\rm Jup}$ larger than predicted by the standard cooling theory of irradiated gas giant planets. We find the retrograde orbit of WASP-17b to be slightly eccentric, with $0.0012 < e < 0.070$ (3σ). Such a low eccentricity suggests that, under current models, tidal heating alone could not have bloated the planet to its current size, so the radius of WASP-17b is currently unexplained. From the measured planet–star flux-density ratios we infer 4.5 and 8 μm brightness temperatures of 1881 ± 50 and 1580 ± 150 K, respectively, consistent with a low-albedo planet that efficiently redistributes heat from its day side to its night side.

Key words: methods: data analysis – techniques: photometric – occultations – planets and satellites: atmospheres – planets and satellites: individual: WASP-17b – stars: individual: WASP-17.

1 INTRODUCTION

WASP-17b is a transiting, 0.49 Jupiter-mass planet in a 3.74-d orbit around a metal-poor, 1.3 solar-mass F6V star (Anderson et al. 2010b, hereafter A10). Data presented in A10, confirmed by Triaud et al. (2010, hereafter T10) and Bayliss et al. (2010), indicated that WASP-17b is in a retrograde orbit around its host star, the first such orbit to be found.

WASP-17b probably formed beyond the ice line in a near-circular, coplanar orbit, as predicted by the canonical model of star and planet formation. It may have subsequently acquired an eccentric, highly inclined orbit via planet–planet scattering (e.g. Ford & Rasio 2008) or the Kozai mechanism (e.g. Fabrycky & Tremaine 2007; Nagasawa, Ida & Bessho 2008). Tidal friction may then have shortened and circularized the long, eccentric orbit, with the energy being dissipated within the planet as heat (e.g. Jackson, Greenberg & Barnes 2008b; Ibgui & Burrows 2009).

As the planet is low mass and the star is hot ($T_{\rm eff} = 6650 \pm 80$ K; T10) and fast rotating ($v \sin I = 9.8\,{\rm km\,s^{-1}}$; T10), the radial velocity (RV) measurements are relatively low signal-to-noise ratio, and so the eccentricity of the planet's orbit was poorly constrained ($e = 0$–0.24) in the discovery paper (A10). This translated into uncertainties in the stellar radius ($R_* = 1.2$–$1.6\,{\rm R}_\odot$) and thus in the planetary radius ($R_{\rm pl} = 1.5$–$2.0R_{\rm Jup}$), meaning the planet is larger than predicted by the standard cooling theory of irradiated gas giant planets by 0.2–$0.7R_{\rm Jup}$ (Fortney, Marley & Barnes 2007).

Using a coupled radius–orbit evolutionary model, Ibgui & Burrows (2009) demonstrated that planets can be inflated to radii of $2R_{\rm Jup}$ and beyond during a transient phase of heating that accompanies the tidal circularization of a short ($a \approx 0.1$ au), highly eccentric ($e \approx 0.8$) orbit. Such a large radius persists for only a few tens of Myr, suggesting that we are unlikely to observe any one system during this brief stage. However, only 3–4 of the ∼100 known planets

⋆E-mail: dra@astro.keele.ac.uk

are extremely bloated and the transit technique does preferentially find large planets.

Leconte et al. (2010) argued that the tidal heating rate is underestimated for even moderately eccentric orbits in studies such as that of Ibgui & Burrows (2009). If true, then a large fraction of energy tidally dissipated within the planet would have been radiated away by the age typical of the most bloated planets (a few Gyr) and so could not have played a significant role in their observed bloating. Ibgui, Spiegel & Burrows (2011) admit that their equations are not applicable at large eccentricity, but counter that neither are those that Leconte et al. (2010) use. They state that the current uncertainty in tidal theory means that no approach can be considered correct.

In A10, the derived radius of WASP-17b is largest ($2.0R_{\rm Jup}$) when a circular orbit is imposed, smaller ($1.7R_{\rm Jup}$) when eccentricity is a free parameter ($e = 0.13$) and smaller again ($1.5R_{\rm Jup}$) when a main-sequence prior is imposed on the star and eccentricity is let free ($e = 0.24$). Ibgui & Burrows (2009) and Ibgui et al. (2011) each note that, compared to planets that did not undergo tidal heating, tidally inflated planets are still significantly larger Gyr after their orbits have circularized and tidal heating has ceased. In each study though, the orbits are still significantly non-circular ($e \gtrsim 0.1$) when the planets are largest. Hence, if the orbit of WASP-17b were found to be near-circular (which would mean that $R_{\rm pl} \approx 2R_{\rm Jup}$) then it would seem unlikely that the planet could have been inflated by a single episode of tidal inflation. Another possibility is an ongoing tidal heating scenario, as explored by Ibgui, Burrows & Spiegel (2010), in which the orbit of WASP-17b would be kept non-circular by the continuing interaction with an as-yet undiscovered third body.

In order to better constrain the stellar and planetary radii, the system age and the potential transient and ongoing tidal heating rates, an improved determination of orbital eccentricity is required. Further high-precision RV measurements were obtained and presented in T10. These allowed eccentricity to be better constrained to $e = 0.066^{+0.030}_{-0.043}$. The best prospect of improving this situation further lay with the measurement of an occultation (as the planet passes behind the star), which would constrain $e \cos \omega$, where ω is the argument of periastron.

In addition, by observing occultations from the ground (e.g. Anderson et al. 2010a) and from space (e.g. Wheatley et al. 2010), we are able to perform photometry and emission spectroscopy of exoplanets which are spatially unresolved from their host stars. This allows us to determine planet albedos and the rates at which energy is redistributed from the day side to the night side of the planet (e.g. Barman 2008), and to infer the temperature structure (e.g. Knutson et al. 2008) and chemical composition of planet atmospheres (e.g. Swain et al. 2009).

We present here observations of two occultations of WASP-17b, each of which was measured at both 4.5 and 8 μm. We combine these new data with existing data in a simultaneous analysis to show that WASP-17b is the largest ($R_{\rm pl} = 2.0R_{\rm Jup}$) and least-dense ($\rho_{\rm pl} = 0.06\,\rho_{\rm Jup}$) planet known, and is in a slightly eccentric orbit around a 2–3 Gyr old F-type star. Exoplanet occultation photometry is at the limit of *Spitzer* systematics and reliable conclusions concerning atmospheres and orbits depend on a careful analysis of the data. We thus present a detailed description of our method.

2 NEW OBSERVATIONS

We observed two occultations of the planet WASP-17b by its $K_{\rm s} = 10.22$ host star with the *Spitzer Space Telescope* (Werner et al. 2004) during 2009 April 24 and 2009 May 1. On each date we measured the WASP-17 system with the Infrared Array Camera (IRAC; Fazio et al. 2004) in full array mode (256 × 256 pixels, 1.2 arcsec pixel^{-1}) simultaneously in channel 2 (4.5 μm) and channel 4 (8 μm) for a duration of 8.4 h. We used an effective integration time of 10.4 s, resulting in 2319 images per channel per occultation. To reduce the time-dependent sensitivity of the 8-μm channel (e.g. Knutson et al. 2008), we exposed the array to a bright, diffuse source (M42) for 214 frames immediately prior to each occultation observation.

We used the images calibrated by the standard *Spitzer* pipeline (version S18.7.0) and delivered to the community as Basic Calibrated Data (BCD). We added back to each image the estimated brightness of the zodiacal light in the sky dark (Reach et al. 2005) so photometric uncertainties and the optimal aperture radii are correctly determined. For each image, we converted flux from MJy sr^{-1} to electrons and then used IRAF to perform aperture photometry for WASP-17, using circular apertures with a range of radii (1–6 pixels). The apertures were centred by fitting a Gaussian profile on the target. The sky background was measured in an annulus extending from 8 to 12 pixels from the aperture centre, and was subtracted from the flux measured within the on-source apertures. We estimated the photometric uncertainty as the quadrature addition of the uncertainty in the sky background in the on-source aperture, the read-out noise and the Poisson noise of the total background-subtracted counts within the on-source aperture. We calculated the mid-exposure times in the HJD (UTC) time system from the MHJD_OBS header values, which are the start times of the Data Collection Events (DCEs), by adding half the integration time (FRAMTIME) values.

We found (see Section 3) that for WASP-17 the highest signal-to-noise ratio is obtained when using an aperture radius of 2.9 pixels for the 4.5 μm data, and a radius of 1.6 pixels for the 8 μm data. The data are displayed raw and binned in the first and second panels, respectively, of Fig. 1.

We rejected any flux measurement that was discrepant with the median of its 20 neighbours (a window width of 4.4 min) by more than four times its theoretical error bar. We also performed a rejection on target position. For each image and for the x and y detector coordinates separately, we computed the difference between the fitted target position and the median of its 20 neighbours. For each data set, we then calculated the standard deviation σ of these *median differences* and rejected any points discrepant by more than 4σ. The numbers of points rejected on flux and target position for each data set are given in Table 1.

According to the IRAC handbook, each IRAC array receives approximately 1.5 solar-proton and cosmic ray hits per second, with ∼2 pixels affected in channel 2, and ∼6 pixels per hit affected in channel 4, while the cosmic ray flux varies randomly by up to a factor of a few over time-scales of minutes. Thus the probability per exposure that pixels within the stellar aperture will be affected by a cosmic ray hit is 1.5 per cent for channel 2 and 1.3 per cent for channel 4, which is in good agreement with the small portion of frames that we rejected.

3 DATA ANALYSIS

3.1 Data and model

We determined the system parameters from a simultaneous analysis incorporating our new *Spitzer* occultation photometry; the WASP discovery photometry covering the full orbit for the three seasons (March to August) of 2006–2008 and presented in A10; a high-precision, $I_{\rm c}$ band transit light curve taken with the 1.2-m Euler-Swiss telescope on 2008 May 6 and presented in A10 and 124 RV

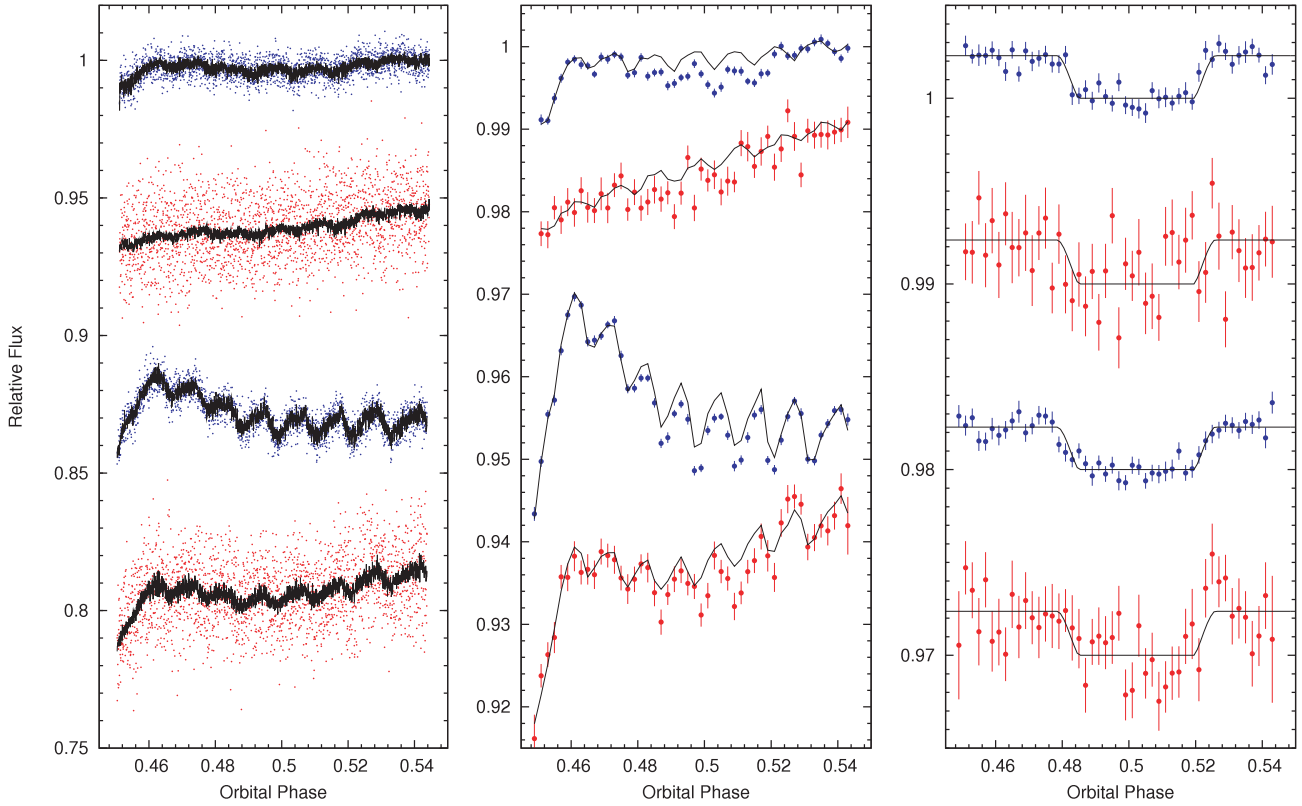

Figure 1. In each of the above three plots, the upper two data sets were obtained at 4.5 μm (blue) and 8 μm (red) on 2009 April 24 and the lower two data sets were taken at 4.5 μm (blue) and 8 μm (red) on 2009 May 1. Relative flux offsets were applied to data sets for clarity. Left: raw *Spitzer* data with the best-fitting trend and occultation models superimposed. Middle: the same data binned in phase ($\Delta\phi = 0.002$, ∼11 min) with the best-fitting trend models superimposed. Right: the binned data after dividing by the best-fitting trend models, and with the best-fitting occultation models superimposed. We normalize the flux received from the star alone to unity, which is measured during occultation.

Table 1. Number of points rejected per data set per criterion.

Data set	Flux	*x*-pos	*y*-pos	Total (per cent)
2009 April 24 / 4.5 μm	34	4	1	35 (1.5)
2009 April 24 / 8 μm	29	31	30	45 (1.9)
2009 May 1 / 4.5 μm	35	6	6	40 (1.7)
2009 May 1 / 8 μm	17	25	22	37 (1.6)

measurements, including 34 taken during transit, made with the CORALIE and HARPS spectrographs and presented in A10 and T10.

These data were input into an adaptive Markov chain Monte Carlo (MCMC) algorithm (Collier Cameron et al. 2007; Pollacco et al. 2008; Enoch et al. 2010). Such a simultaneous analysis is necessary to take account of the cross-dependency of system parameters and to make an honest assessment of their uncertainties. We used the following as MCMC proposal parameters: T_c, P, ΔF, T_{14}, b, K_1, $T_{\rm eff}$, [Fe/H], $\sqrt{e}\cos\omega$, $\sqrt{e}\sin\omega$, $\sqrt{v\sin I}\cos\lambda$, $\sqrt{v\sin I}\sin\lambda$, $\Delta F_{4.5\,\mu\rm m}$ and $\Delta F_{8\,\mu\rm m}$ (see Table 5 for definitions).

At each step in the MCMC procedure, each proposal parameter is perturbed from its previous value by a small, random amount. Stellar density, which is constrained by the shape of the transit light curve (Seager & Mallén-Ornelas 2003) and the eccentricity of the orbit, is calculated from the proposal parameter values. This is input, together with the latest values of $T_{\rm eff}$ and [Fe/H] (which are controlled by Gaussian priors) into the empirical mass calibration of Enoch et al. (2010) to obtain an estimate of the stellar mass M_*. From the proposal parameters, model light and RV curves are generated and χ^2 is calculated from their comparison with the data. A step is accepted if χ^2 (our merit function) is lower than for the previous step, and a step with higher χ^2 is accepted with probability $\exp(-\Delta\chi^2/2)$. In this way, the parameter space around the optimum solution is thoroughly explored. The value and uncertainty of each parameter are, respectively, taken as the median and central 68.3 per cent confidence interval of the parameter's marginalized posterior probability distribution.

As Ford (2006) notes, it is convenient to use $e\cos\omega$ and $e\sin\omega$ as MCMC proposal parameters, because these two quantities are nearly orthogonal and their joint probability density function is well behaved when the eccentricity is small and ω is highly uncertain. Ford cautions, however, that the use of $e\cos\omega$ and $e\sin\omega$ as proposal parameters implicitly imposes a prior on the eccentricity that increases linearly with e. As such, we instead use $\sqrt{e}\cos\omega$ and $\sqrt{e}\sin\omega$ as proposal parameters, which restores a uniform prior on e. For similar reasons, we use $\sqrt{v\sin I}\cos\lambda$ and $\sqrt{v\sin I}\sin\lambda$ rather than $v\sin I\cos\lambda$ and $v\sin I\sin\lambda$ to parametrize the Rossiter–McLaughlin effect (e.g. Gaudi & Winn 2007).

3.2 *Spitzer* data

3.2.1 *Deciding between models and data sets*

Systematics are present in IRAC photometry at a level similar to the predicted planetary occultation signal. Therefore, it is necessary to carefully detrend the photometry so as to obtain accurate occultation

depths and timings. To discriminate between various detrending models we used the Bayesian information criterion (BIC; Schwarz 1978):

$$\mathrm{BIC} = \chi^2 + k \ln N, \quad (1)$$

where k is the number of free model parameters and N is the number of data points. The BIC prefers simpler models unless the addition of extra terms significantly improves the fit. As such, it is a useful tool for selecting between models with different numbers of free parameters.

In addition, we used the root mean square (rms) of the residuals about the best-fitting trend and occultation models to discriminate between different light curves obtained from different reductions of the same sets of images.

3.2.2 Aperture radii

We determined the optimal aperture radii to use for the 4.5 and 8 μm data by performing aperture photometry with a range of aperture radii (1–6 pixels), and choosing the radii that produced the maximal signal-to-noise ratio (Fig. 2; e.g. Howell 1989).

For the 4.5 μm data, the radius that results in the highest signal-to-noise ratio is 2.9 pixels and it is this radius that we adopt (Fig. 2, upper panel). This radius incorporates the majority (∼92.5 per cent) of the target flux and little background flux (∼2.6 per cent of that of the target).

At 8 μm, as compared to 4.5 μm, the background is brighter by a factor of ∼20 and the source is fainter by a factor of ∼4. Thus, with increasing aperture radius, the background flux quickly dominates the target flux (Fig. 2, lower panel). Indeed, the background flux equals the target flux when using our adopted, optimal (highest signal-to-noise ratio) radius of only 1.6 pixels. This radius incorporates ∼60 per cent of the target flux and a similar amount (97 per cent of the target) of background flux. The background flux is greater than the target flux by factors of ∼1.5, 2, 3 and 7.5 within apertures with radii of 2.2, 2.75, 3.5 and 6 pixels, respectively.

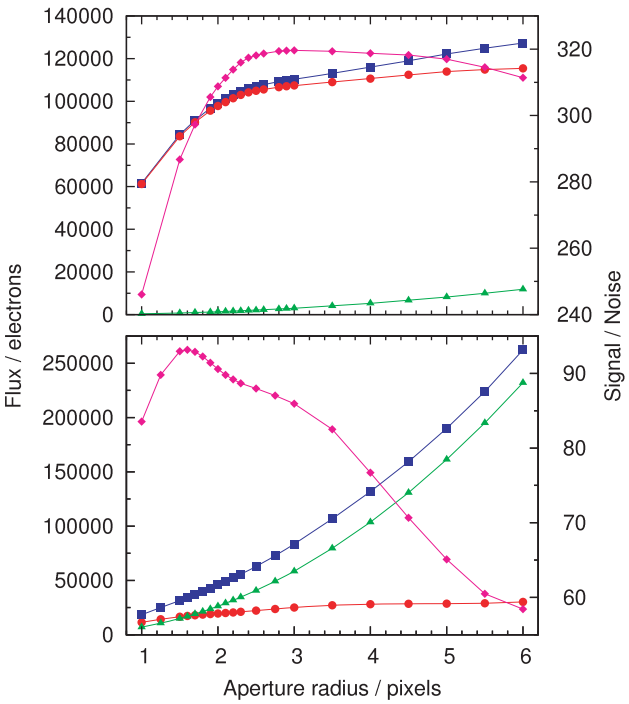

Figure 2. The flux due to WASP-17 (red circles), the sky and instrumental background (green triangles) and both WASP-17 and the background combined (blue squares), as well as the signal-to-noise ratio (magenta diamonds) as a function of aperture radius. The upper and lower panels show the 4.5 and 8 μm data, respectively. We show the data from 2009 April 24, but the data from 2009 May 1 produce near-identical plots.

3.2.3 Systematics

IRAC uses an InSb detector to detect light around 4.5 μm, and the measured flux exhibits a strong correlation with the position of the target star on the array. This effect is due to the inhomogeneous intrapixel sensitivity of the detector and is well documented (e.g. Knutson et al. 2008, and references therein). Following Charbonneau et al. (2008) we modelled this effect as a quadratic function of the subpixel position of the point spread function (PSF) centre, but with the addition of a linear term in time:

$$\mathrm{d}f = a_0 + a_x\,\mathrm{d}x + a_y\,\mathrm{d}y + a_{xx}\,\mathrm{d}x^2 + a_{yy}\,\mathrm{d}y^2 + a_t\,\mathrm{d}t, \quad (2)$$

where $\mathrm{d}f = f - \hat{f}$ is the stellar flux relative to its weighted mean, $\mathrm{d}x = x - \hat{x}$ and $\mathrm{d}y = y - \hat{y}$ are the coordinates of the PSF centre relative to their weighted means, $\mathrm{d}t$ is the time since the beginning of the observation and a_0, a_x, a_y, a_{xx}, a_{yy} and a_t are coefficients. We determined the trend model coefficients by linear least-squares minimization at each MCMC step, subsequent to division of the data by the eclipse model. We used singular value decomposition (Press et al. 1992) for this purpose. Though a common eclipse model was fitted to occultation data from the same channel, trend models were fitted separately to each data set.

The best-fitting trend models are superimposed on the binned photometry in the middle panel (first and third curves from the top) of Fig. 1. Table 2 gives the best-fitting values for the trend model parameters (equation 2), together with their 1σ uncertainties.

We found consistent 4.5 μm eclipse depths when incorporating one of the two data sets or both of them in our analysis: $\Delta F_{4.5\,\mu\mathrm{m}_1} = 0.00225 \pm 0.00015$, $\Delta F_{4.5\,\mu\mathrm{m}_2} = 0.00244 \pm 0.00020$ and $\Delta F_{4.5\,\mu\mathrm{m}_{1+2}} = 0.00230 \pm 0.00012$.

The systematics in the data from 2009 April 24 are of much smaller amplitude than those in the data from 2009 May 1. This is due to a chance placement of the target star on the detector. The detector positions of WASP-17's PSF centre are shown in Fig. 3. During each occultation and in each channel the motion due to the nodding of the spacecraft is evident in the x and y positions of the PSF centres. However, contrasting the two occultations, there is a marked difference in the radial distance from the nearest pixel centre over the course of the observations. In the data from 2009 April 24 the placement of the target on the detectors is such that the motion of the spacecraft in the x-direction largely compensates

Table 2. Trend model parameters and coefficients.

	4.5 μm		8 μm	
	2009 April 24	2009 May 1	2009 April 24	2009 May 1
$\hat{f}$	106 955.09	107 395.47	17 289.49	17 866.66
$\hat{x}$	24.28	24.85	25.23	25.64
$\hat{y}$	25.28	25.44	23.02	23.18
a_0	$-26.0^{+3.6}_{-3.8}$	$-10.8^{+10.7}_{-10.4}$	$-108.42^{+0.67}_{-0.77}$	$-94.2^{+3.1}_{-3.1}$
a_x	$-2606.7^{+13.1}_{-13.3}$	$4927.2^{+61.1}_{-60.5}$	$720.2^{+6.5}_{-6.2}$	$-142.0^{+19.1}_{-20.1}$
a_y	$-5049.5^{+20.2}_{-20.3}$	$-6866.5^{+11.9}_{-11.6}$	$42.3^{+5.2}_{-4.9}$	$-1301.6^{+7.7}_{-7.2}$
a_{xx}	$8345.6^{+479.7}_{-487.6}$	$-105.0^{+636.2}_{-661.9}$	$-1368.7^{+114.6}_{-110.7}$	$-1748.4^{+401.7}_{-398.4}$
a_{yy}	$-8340.8^{+385.5}_{-416.0}$	$3663.4^{+155.7}_{-165.5}$	$-1246.8^{+136.0}_{-134.3}$	$905.4^{+122.2}_{-121.2}$
a_t	$207.7^{+20.7}_{-19.2}$	$-14.5^{+35.8}_{-37.0}$	$648.9^{+5.2}_{-4.9}$	$557.7^{+9.0}_{-9.1}$

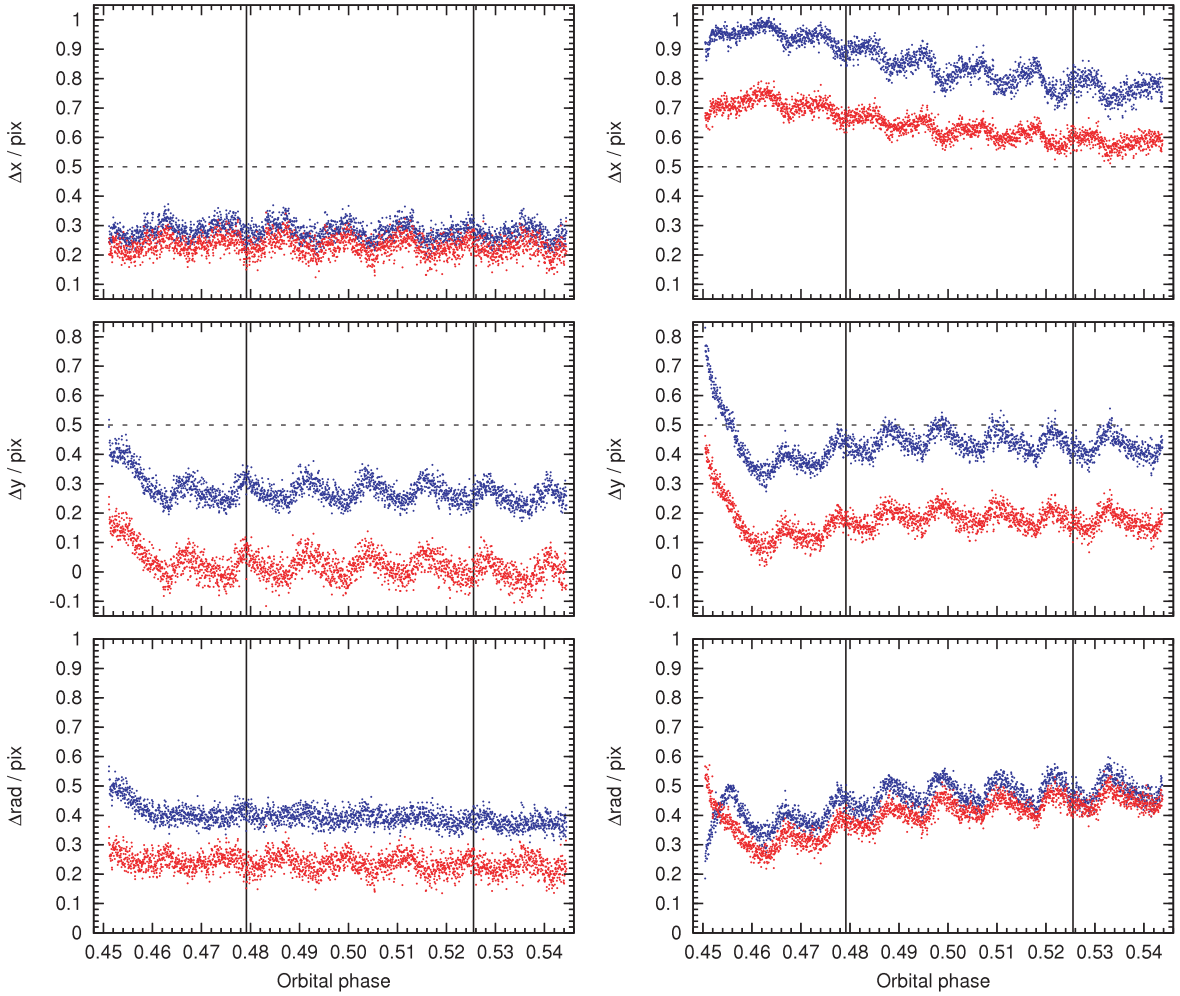

Figure 3. The detector positions of WASP-17's PSF centre for the first occultation (left-hand plots) and the second occultation (right-hand plots). The PSF centre positions on the 4.5 and 8 μm detectors are, respectively, depicted by blue and red dots. For each occultation we show the distance of the PSF centre from the nearest pixel centre in the x and y directions (top and middle panels, respectively) and in the radial direction (bottom panels). Pixel centres are located at $(x, y) = (0, 0)$, while pixel edges are located at (0.5, 0.5) and are demarcated by dashed lines.

for the motion in the y-direction, resulting in a near constant radial distance from the nearest pixel centre. The opposite is the case in the 2009 May 1 data set, where the motion in the x and y directions combines to produce large-amplitude oscillations in the distance from the nearest pixel centre. This results in the large saw-tooth systematics seen in the light curve (second panel of Fig. 1).

Near the beginning of the observations on 2009 May 1, the target crossed a pixel boundary on the 4.5 μm detector (Fig. 3, middle right-hand plot). This resulted in a point of inflection in the distance of the target from the nearest pixel centre (Fig. 3, bottom right-hand plot). As the sensitivity is higher toward the pixel centre and lower near the edges, it is therefore curious that no corresponding inflection point is seen in the light curve (Fig. 1, middle panel).

IRAC uses a SiAs detector to observe at 8 μm, and its response is usually thought to be homogeneous, though another systematic affects the photometry. This effect is known as the 'ramp' because it causes the gain to increase asymptotically over time for every pixel, with an amplitude depending on a pixel's illumination history (e.g. Knutson et al. 2008, and references therein). Again following Charbonneau et al. (2008), we modelled this ramp as a quadratic function of $\ln(\mathrm{d}t)$:

$$\mathrm{d}f = a_0 + a_1 \ln(\mathrm{d}t + t_{\mathrm{off}}) + a_2(\ln(\mathrm{d}t + t_{\mathrm{off}}))^2, \quad (3)$$

where t_{off} is a proposal parameter. To prevent t_{off} from drifting more than an hour or so prior to the first observation, we place on it a Gaussian prior by adding a Bayesian penalty to our merit function (χ^2):

$$\mathrm{BP}_{t_{\mathrm{off}}} = t_{\mathrm{off}}^2/\sigma_{t_{\mathrm{off}}}^2, \quad (4)$$

where $\sigma_{t_{\mathrm{off}}} = 15$ min.

From an initial MCMC run, we observed systematics in the residuals of the second 8 μm data set, and so investigated decorrelating the 8 μm data with detector position. A significantly lower occultation BIC ($\Delta\mathrm{BIC} = -141$) resulted when also detrending for detector position, i.e. detrending with equation (2) rather than with equation (3). In addition, there was less scatter in the 8 μm data when decorrelating with detector position (i.e. when detrending with equation 2 rather than with equation 3; Fig. 4 and Table 3). When not decorrelating with detector position, significantly different best-fitting 8 μm occultation depths were obtained for the two individual data sets (Table 3) and the depth obtained from the combined data sets was much deeper than otherwise. For these reasons and for reasons that will be presented in the remainder of this section, we opted to decorrelate the 8 μm data with detector position.

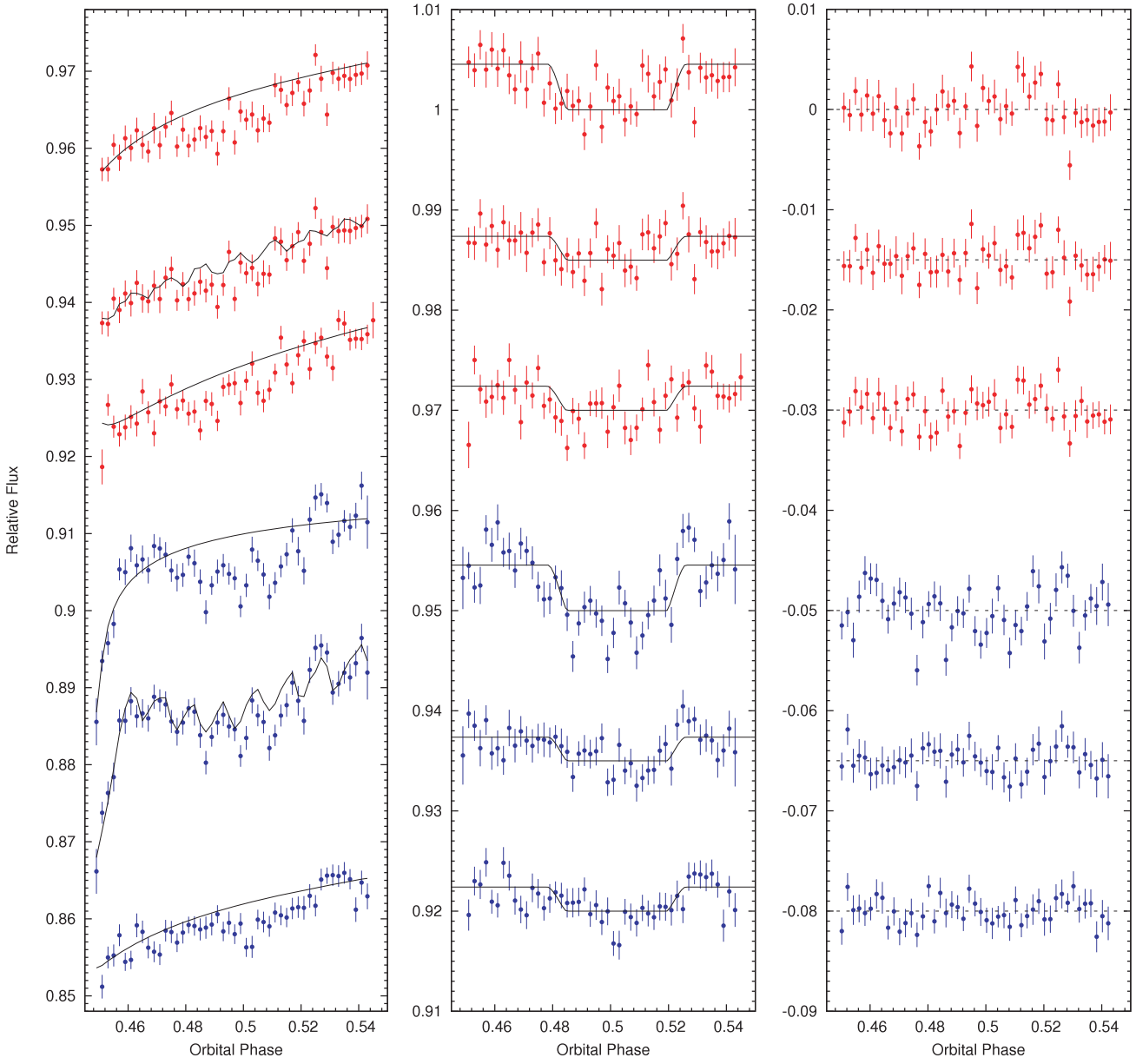

Figure 4. A comparison of the methods for reducing and detrending the 8 μm data. In each of the above three panels, the upper three curves (red dots) are the data from 2009 April 24 and the lower three curves (blue dots) are the data from 2009 May 1. In each triplet of curves, the top curve is the light curve obtained by aperture photometry and detrended with equation (3). The middle curve is the light curve obtained by aperture photometry and detrended with equation (2). The bottom curve is the light curve obtained by deconvolution photometry and detrended with equation (3). Left-hand panel: binned raw data, with the best-fitting trend models superimposed. Middle panel: binned detrended data, with the best-fitting occultation models superimposed. Right-hand panel: binned residuals about the best-fitting trend and occultation models.

Table 3. A comparison of the 8 μm occultation depths and residuals from deconvolution photometry and aperture photometry.

Method	Trend eq.	$\Delta F_{8\,\mu m_{1+2}}$	$\Delta F_{8\,\mu m_1}$	$\Delta F_{8\,\mu m_2}$	$rms_{8\,\mu m_{1+2}}$	$rms_{8\,\mu m_1}$	$rms_{8\,\mu m_2}$
Aper. phot.	2	0.00238 ± 0.00036	0.00187 ± 0.00050	0.00303 ± 0.00059	0.01103	0.01142	0.01010
Aper. phot.	3	0.00455 ± 0.00036	0.00246 ± 0.00058	0.00643 ± 0.00055	0.01112	0.01127	0.01119
Decon. phot.	3	0.00240 ± 0.00036	0.00202 ± 0.00052	0.00276 ± 0.00047	0.00994	0.01019	0.00967

In Section 3.3 we use deconvolution photometry to show that the observed dependence on detector position is likely to have been introduced during aperture photometry. Therefore, there is no evidence of an inhomogeneous intrapixel response of the SiAs 8 μm detector, contrary to the case with the InSb 4.5 μm detector.

The second and fourth curves from the top in the middle panel of Fig. 1 are the best-fitting trend models when detrending the two

Table 4. The 8 μm occultation depths and the combined (4.5 and 8 μm) relative occultation BIC values, when detrending the 8 μm data with the various models.

Model	Eq.	$\Delta F_{8\,\mu\mathrm{m}_{1+2}}$	$\Delta F_{8\,\mu\mathrm{m}_1}$	$\Delta F_{8\,\mu\mathrm{m}_2}$	$\Delta\mathrm{BIC}_{8\,\mu\mathrm{m}_{1+2}}$	$\Delta\mathrm{BIC}_{8\,\mu\mathrm{m}_1}$	$\Delta\mathrm{BIC}_{8\,\mu\mathrm{m}_2}$
Linear time[a]	2	0.00238 ± 0.00036	0.00187 ± 0.00045	0.00307 ± 0.00055	0	0	0
Quad ln time	8	0.00271 ± 0.00042	0.00226 ± 0.00060	0.00329 ± 0.00063	14	38	31
Quad time	6	0.00291 ± 0.00059	0.00179 ± 0.00085	0.00397 ± 0.00086	16	17	15
Rising exp	9	0.00260 ± 0.00037	0.00188 ± 0.00047	0.00307 ± 0.00055	17	17	17
Linear ln time	7	0.00363 ± 0.00038	0.00318 ± 0.00046	0.00417 ± 0.00054	60	34	25
No time	5	0.00210 ± 0.00037	0.00103 ± 0.00046	0.00353 ± 0.00058	252	210	18

[a]For Linear time: $\mathrm{BIC}_{4.5\,\mu\mathrm{m}_{1+2}+8\,\mu\mathrm{m}_{1+2}} = 10\,772$, $\mathrm{BIC}_{4.5\,\mu\mathrm{m}_{1+2}+8\,\mu\mathrm{m}_1} = 8298$ and $\mathrm{BIC}_{4.5\,\mu\mathrm{m}_{1+2}+8\,\mu\mathrm{m}_2} = 8072$.

8 μm data sets with equation (2). Note that the saw-tooth patterns of the 8 μm trend models are in phase with those of the 4.5 μm trend models, though each data set was fit separately with its own trend model.

In addition to equation (2), which we will call *linear time*, we tried trend functions with a variety of time dependency. These were *no time*:

$$\mathrm{d}f = \mathrm{spatial}, \tag{5}$$

where $\mathrm{spatial} = a_0 + a_x\,\mathrm{d}x + a_y\,\mathrm{d}y + a_{xx}\,\mathrm{d}x^2 + a_{yy}\,\mathrm{d}y^2$ represents the detector position terms and an offset; *quad time*:

$$\mathrm{d}f = \mathrm{spatial} + a_t\,\mathrm{d}t + a_{tt}\,\mathrm{d}t^2; \tag{6}$$

linear ln time:

$$\mathrm{d}f = \mathrm{spatial} + a_1 \ln(\mathrm{d}t + t_{\mathrm{off}}); \tag{7}$$

quad ln time:

$$\mathrm{d}f = \mathrm{spatial} + a_1 \ln(\mathrm{d}t + t_{\mathrm{off}}) + a_2(\ln(\mathrm{d}t + t_{\mathrm{off}}))^2 \tag{8}$$

and *rising exp* (Harrington et al. 2007):

$$\mathrm{d}f = \mathrm{spatial} + a_3 \exp(a_4\,\mathrm{d}t), \tag{9}$$

where a_4 is a proposal parameter.

In Table 4 we present the occultation depths and BIC values resulting from detrending the 8 μm data with the various models. The 4.5 and 8 μm data were fitted simultaneously, so an improved fit to the 8 μm data would not be preferred if the fit to the 4.5 μm data were considerably worse. In Table 4 the models are presented in descending order by how well they fit the combined 8 μm data sets ($8\,\mu\mathrm{m}_{1+2}$), and the BIC values are given relative to the best-fitting model (*linear time*). The *linear time* model is strongly favoured and we thus adopt this as our trend model for the 8 μm data. The BIC values resulting from MCMC runs incorporating the two 8 μm data sets individually ($8\,\mu\mathrm{m}_1$ and $8\,\mu\mathrm{m}_2$) are also given, with a similar order of preference to that of the combined data sets. Again, the *linear time* model is clearly favoured over the others, supporting our decision to use the same model for the two data sets. The occultation depths are consistent between the four most preferred models, but are not so for the two less preferred models. The depths found from the first data set are shallower than those found from the second data set, with a difference between the two of 1.7σ in the case of the *linear time* trend model.

In Fig. 5 we present the detector positions of WASP-17 both during and outside of occultation. On 2009 April 24, the star occupied the same region of the detector during the occultation as when outside of occultation. However, on 2009 May 1, the star occupied different regions of the detector during occultation than when outside of occultation, though there was some overlap. The reason for this can be seen in the top right-hand panel of Fig. 3, which shows that the star moved steadily in the x-direction. This was in addition to the motion due to the nodding of the spacecraft, which resulted in some overlap between the in-occultation and out-of-occultation detector positions. As we decorrelate the light curves with detector

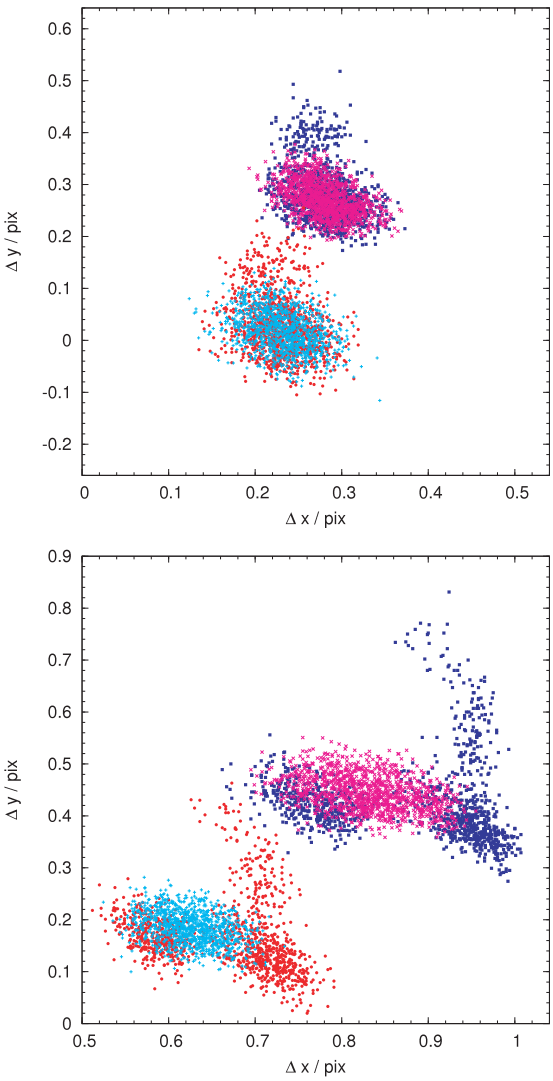

Figure 5. The detector positions of WASP-17 both during and outside of occultation. The top panel shows the occultation of 2009 April 24 and the bottom panel shows the occultation of 2009 May 1. The 4.5 μm (blue squares) and 8 μm (red circles) data taken outside of occultation are overplotted with the 4.5 μm (magenta saltires) and 8 μm (cyan crosses) data taken during occultation. The 4.5 μm data are shown relative to detector position $(x, y) = (24, 25)$, and the 8 μm relative to $(x, y) = (25, 23)$. Note that, though the axes' ranges are the same between the two plots, each abscissa covers only 60 per cent the range of each ordinate.

position, the data from 2009 April 24, with the greater detector position overlap, are thought to be more reliable. However, the data from the two occultations detrend similarly well, and we find no reason to disregard the latter data set. This indicates that, though we had requested the same detector positions for the target for each observation run, small differences in the pointing and motion of *Spitzer* can result in markedly different systematics.

We investigated using the fitted PSF positions from the higher signal-to-noise ratio 4.5 μm data in the aperture photometry and positional decorrelation of the 8 μm data. To account for the offset between the two detectors we fit the differences in the x and y directions and translated the coordinates by those amounts. The 8 μm occultation depths, both when incorporating one of the two data sets or both of them, were very similar to those obtained when fitting the stellar PSF position in the 8 μm data, and there was no significant reduction in the residual scatter about the best-fitting models. Hence, we proceeded as before.

Spitzer's pointing oscillates around the nominal position, with an amplitude of ∼0.1 pixels over a period of ∼1 h. We also see higher frequency jitter, with periods of 1–2 min (the cadence of our data is 12 s), in the position of WASP-17. Some authors (e.g. Wheatley et al. 2010) chose to smooth the measured target positions prior to light-curve detrending. However, we found that detrending with the unsmoothed positions resulted in a reduced BIC ($\Delta\mathrm{BIC} = -931$), and in smaller residual rms values: 5.3 and 8.8 per cent lower for the two 4.5 μm data sets, and 0.6 and 1.4 per cent lower for the two 8 μm data sets.

To ascertain whether the observed short-period jitter was due to measurement error, we measured the position of a second star in the field for the two 4.5 μm data sets. For both WASP-17 and the second star we subtracted their Gaussian-smoothed ($\sigma = 84$ s) positions to remove the longer period oscillations. We then fitted Gaussians to the distributions of the detector x and y coordinates of both stars and of their relative separations. If the measured positions of WASP-17 and the second star are uncorrelated, then the variance of the distribution of relative separations would be the sum of the variances of the distributions of each star's positions. However, we found that the distribution of separation in the x-direction had a variance smaller than that by a factor of 9 for the first data set and by a factor of 2 for the second data set. For the y-coordinate, the factors were 25 and 6 for the two data sets. Thus, the short-period jitter is real and the light curves should be detrended with unsmoothed target positions.

3.2.4 *Aperture radii revisited*

As a check of the choice of aperture radius (2.9 pixels) for the 4.5 μm data, we input the 4.5 μm light curves obtained with each aperture radius into a simultaneous MCMC analysis that incorporated all but the 8 μm data. These analyses produced consistent 4.5 μm occultation depths (Fig. 6, upper panel), indicating that the 4.5 μm result is relatively insensitive to the choice of aperture radius.

As a check of the choice of aperture radius (1.6 pixels) for the 8 μm data, we input each 8 μm light curve into a simultaneous MCMC analysis that incorporated all other data. When decorrelating with detector position (Fig. 6, middle panel), the fitted 8 μm occultation depth varies weakly with aperture radius. Beyond an aperture radius of 3.5 pixels (by which point the flux due to the sky background is three times that of the target within the target aperture), a deeper occultation is measured. Without decorrelating with detector position (Fig. 6, lower panel), the fitted 8 μm occultation depth is a strong function of aperture radius.

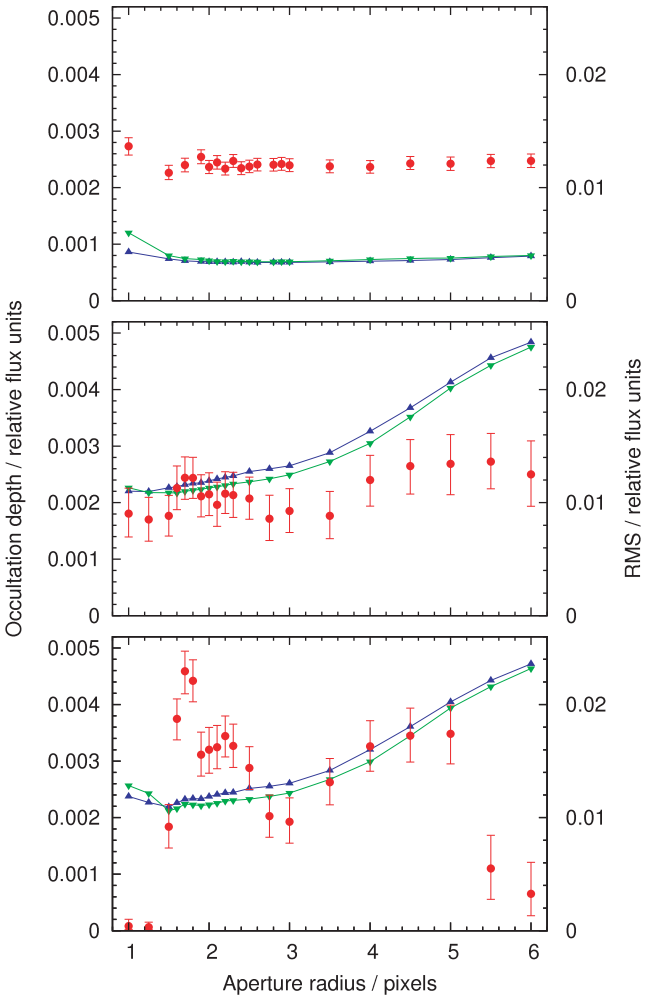

Figure 6. Top panel: the dependence on aperture radius of the fitted occultation depth (red circles with error bars) and the residuals (blue up-triangles = 2009 April 24 data, green down-triangles = 2009 May 1 data) for the 4.5 μm data. Middle panel: the same as the top panel, but for the 8 μm data and when treating the 'pixel phase' effect. Lower panel: the same as the top panel, but for the 8 μm data and when neglecting the 'pixel phase' effect.

As the conclusions drawn from *Spitzer* occultation observations depend on accurately measured occultation depths, we advise others to check for a correlation between flux and detector position in their 5.8 and 8 μm data sets, and for a dependence of occultation depth on aperture radius. For example, from fig. 1 of Fressin et al. (2010) it appears that similar patterns of saw-tooth systematics are present in both the 4.5 and 8 μm light curve, though they only decorrelate the former light curve with detector position. If a dependence of measured flux on detector position was introduced during aperture photometry, then the measured 8 μm occultation depth could be erroneous.

3.3 Deconvolution photometry

To verify the 8 μm occultation depths and to investigate the source of the dependence of the measured 8 μm flux on detector position, we obtained 8 μm light curves by performing deconvolution

photometry with DECPHOT. This method was first described by Gillon et al. (2006, 2007) and has been optimized for *Spitzer* data by Lanotte et al. (in preparation). It is based on the image-deconvolution method of Magain, Courbin & Sohy (1998, see also Magain et al. 2007), which respects the sampling theorem of Shannon (1949), in contrast with traditional deconvolution methods. In a first step, 25 random BCD images taken on 2009 April 24 were used to determine a partial PSF. This was then used to deconvolve the whole set of images and to determine optimally the position and flux of WASP-17.

The DECPHOT light curves do not exhibit a position-dependent modulation of the flux (Fig. 4). Therefore, the saw-tooth modulation seen in the light curves obtained from aperture photometry (Fig. 4) is likely due to a pixellation effect rather than an intrapixel inhomogeneity in IRAC's 8 μm detector response. During aperture photometry of the 8 μm data, an aperture radius of only 1.6 pixels was used. The calculation of a circular aperture is non-trivial and the majority of photometry routines make a polygonal approximation, which tends to be less accurate for smaller radii. Aside from that, the calculation of how much flux should be attributed to partial pixels is another potential source of error. A better result is obtained if a PSF is used, rather than if uniform illumination is assumed, but even that is not perfect. Partial deconvolution is a photometric method that is optimal in a least-squares sense, i.e. the background contribution is minimized because each pixel is properly weighted. As this is not the case for aperture photometry, and as the background at 8 μm is bright relative to the target, we had to use a small aperture to optimize the signal-to-noise ratio of our measurements, leading to pixelization effects that translated into a correlation of the measured flux with detector position.

We performed a combined MCMC analysis incorporating the DECPHOT 8 μm light curves, which were detrended with equation (3). The raw and detrended data are shown with the best-fitting trend and occultation models in Fig. 4. We found consistent 8 μm occultation depths when incorporating only one data set or both data sets in our analysis (Table 3). The residuals of the DECPHOT light curves exhibit a slightly smaller scatter than the aperture photometry light curves do (Fig. 4 and Table 3). These DECPHOT depths and associated uncertainties are in close agreement with those derived using the light curves obtained from simple aperture photometry (Table 3). This is also the case for $e\cos\omega$, $e\sin\omega$ and the time of mid-occultation (Table 6). Thus our method of obtaining 8 μm light curves by simple aperture photometry and detrending them with detector position is verified, and it is these light curves that we use in the simultaneous analysis from which we calculated our system parameter values.

3.4 Partitioning of data

In our simultaneous MCMC analysis we partitioned the WASP photometry according to observation season and camera into five data sets, so that each data set could thus be normalized independently, as was done in A10. As in T10, we partitioned the RV data into four data sets: CORALIE data sampling the full orbit ($rv1$); HARPS data sampling the full orbit ($rv2$); a spectroscopic transit and a week of adjoining data as measured by CORALIE ($rv3$) and a spectroscopic transit and two RVs from the following day as measured by HARPS ($rv4$). Both an instrumental offset and a specific stellar activity level have the potential to affect the measured RV of a star. The spectroscopic transits comprise a large number of RVs taken in quick succession, whereas the data sampling the full orbit were taken over a long time-span and are thus expected to sample a range of stellar activity level that should average to a mean value of zero (T10). Thus, by partioning the RV data, we allow each data set to have its own centre-of-mass velocity γ, thus avoiding the risk of obtaining spurious values for the planet's mass and orbital eccentricity.

3.5 Photometric and RV noise

We scaled the photometric error bars so as to obtain a reduced χ^2 of unity, applying one scale factor per data set. The aim was to properly weight each data set in the simultaneous MCMC analysis and to obtain realistic uncertainties. For the five sets of WASP photometry the scale factors were in the range 0.87–0.96. The error bars of the Euler photometry were multiplied by 1.33. The scale factors for the occultation photometry were in the range 1.04–1.09. Importantly, the error bars of the occultation photometry were not scaled when deciding which trend models or aperture radii to use.

We assessed the presence of correlated noise in the *Spitzer* and Euler data by plotting the rms of their binned residuals (Fig. 7). Though there is no correlated noise evident in the *Spitzer* data, it is present at a small level in the Euler data over time-scales of 8–80 min. Because of the similarity with the time-scales of the fitted features in the transit (ingress takes 36 min, as does egress, and the transit duration is 264 min), the values of some fitted parameters may be affected to a small degree.

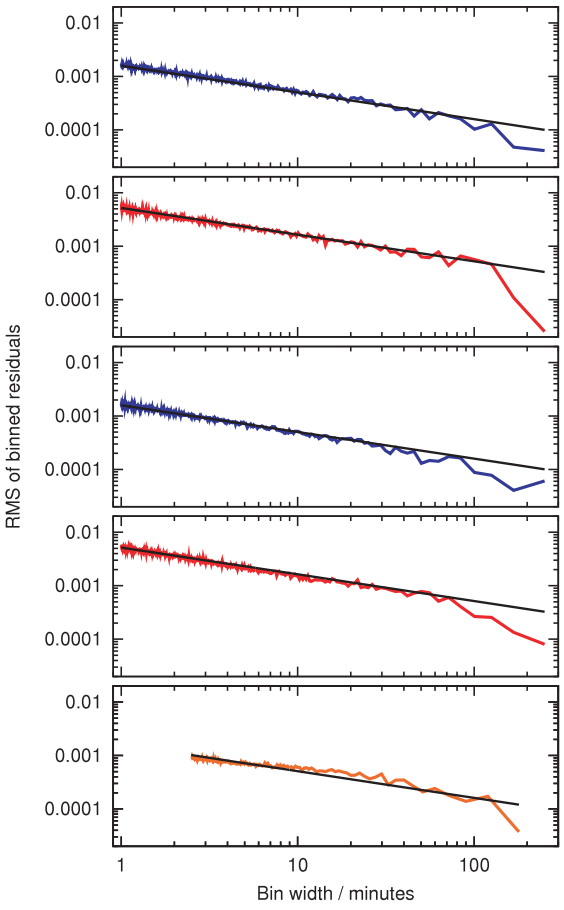

Figure 7. RMS of the binned residuals for the new *Spitzer* occultation photometry (upper four panels, with the data sets presented in the same order as in Fig. 1) and the existing Euler photometry (lower panel). The solid black lines, which are the rms of the unbinned data scaled by the square root of the number of points in each bin, show the white-noise expectation. The ranges of bin widths (1–250 min for *Spitzer* and 2.5–180 min for Euler) are appropriate for the data sets' cadences and durations.

For the same reasons as with the photometry, we added a jitter term in quadrature to the formal RV errors, as might arise from stellar activity. We used an initial MCMC run to determine the level of jitter required for each data set to obtain a reduced χ^2 of unity. We found that the HARPS orbital data ($rv2$) required a jitter of $3\,\mathrm{m\,s^{-1}}$ and the HARPS spectroscopic transit data ($rv4$) required a jitter of $20\,\mathrm{m\,s^{-1}}$. It was not necessary to add any jitter to either of the two CORALIE data sets.

3.6 Time systems and light traveltime

The Euler photometry and the CORALIE RVs are in the BJD (UTC) time system. The WASP and *Spitzer* photometry are in the HJD (UTC) time system. The difference between BJD and HJD is less than 4 s and so is negligible for our purposes. Although leap second adjustments are made to the UTC system to keep it close to mean solar time, meaning one should really use terrestrial time, our observations span a short baseline (2006–2008), during which there were no leap second adjustments.

The occultation of WASP-17b occurs farther away from us than its transit does, so we made a first-order correction for the light traveltime. We calculated the light traveltime between the beginning of occultation ingress and the beginning of transit ingress to be 50.4 s. We subtracted this from the mid-exposure times of the *Spitzer* occultation photometry. As we measure the time of mid-occultation to a precision of ± 150 s, the impact of this correction was small.

4 RESULTS

Table 5 shows the median values and the 1σ uncertainties of the fitted proposal parameters and derived parameters from our final MCMC analysis. Fig. 1 shows the best-fitting trend and occultation models together with the raw and detrended *Spitzer* data. Table 2 gives the best-fitting values for the parameters of the trend models (equation 2), together with their 1σ uncertainties. Fig. 8 displays all the photometry and RVs used in the MCMC analysis, with the best-fitting eclipse and RV models superimposed.

From this we see that WASP-17b is a very bloated planet ($R_{\rm pl} = 2.0 R_{\rm Jup}$) in a slightly eccentric, 3.7 d, retrograde orbit around an F6V star. By constraining the eccentricity of WASP-17b's orbit to low values we have shown that the circular solution presented in A10 (in which a total of three solutions were presented) is closest to reality.

4.1 Orbital eccentricity

We have shown the orbit of WASP-17b to be non-circular: $e\cos\omega$ is non-zero at the 4.8σ level ($e\cos\omega = 0.00352^{+0.00076}_{-0.00073}$; Fig. 9), and the best-fitting solution suggests that WASP-17b is occulted by its host star 12.0 ± 2.5 min later than if it were in a circular orbit. Our measurement of $e\cos\omega$ rules out large values of e for all orbital orientations other than those with $|\omega| \approx 90$, and the limits we place on $e\sin\omega$ prohibits large values of e for those orientations with $|\omega| \approx 90$ (Fig. 10). From the MCMC analysis, the 1σ (68.3 per cent) lower and upper limits on e are, respectively, 0.010 and 0.043, and the 3σ (99.7 per cent) lower and upper limits on e are, respectively, 0.0019 and 0.0701. We can set a more stringent 3σ lower limit on e by assuming $e\sin\omega \approx 0$ (and so $|\omega| \approx 90$), in which case it would be equal to that of the 3σ lower limit on $e\cos\omega$: 0.0012.

Almost all values of ω are permitted by the current data, with only $|\omega| \approx 90$ being ruled out by the limits placed on $e\sin\omega$ (Fig. 10). Large values of e are consistent with the data only if $|\omega| \approx 90$, otherwise any orientation of the orbital major axis is permitted providing that e is small. We can thus use our measurement of $e\cos\omega$ to infer a *probable* value of e. For random orientations of the major axis, the *expected value* of $\cos\omega$ is $E(\cos\omega) = 2/\pi$. Thus, the *expected value* of e is $E(e) = e\cos\omega / E(\cos\omega) = 0.0055$.

We explored the effect of each occultation photometry data set in turn on the orbital eccentricity, and of all four data sets combined. We did so by performing MCMC runs that incorporated either all, none or just one of the *Spitzer* data sets (Table 6 and Fig. 9). This demonstrates how valuable the *Spitzer* occultation photometry is in determining orbital eccentricity, as its inclusion in our combined analysis caused the size of the 68.3 per cent confidence interval for $e\cos\omega$ to decrease by a factor of 30.2, and the interval for $e\sin\omega$ to decrease in size by a factor of 2.4. In addition to the RV data, it is the orbital phase of the occultation that constrains $e\cos\omega$ and it is the occultation duration, relative to the transit duration, that constrains $e\sin\omega$ (Charbonneau et al. 2005). When including any one of the four occultation data sets, the best-fitting values of $e\cos\omega$ and $e\sin\omega$ obtained are consistent with the values obtained when including all four data sets. Thus no individual data set is biasing our best-fitting solution.

5 DISCUSSION

5.1 Planet radius

With a radius of $2.0 R_{\rm Jup}$, WASP-17b is the largest known planet by a margin of $0.2 R_{\rm Jup}$, and is over $0.7 R_{\rm Jup}$ larger than predicted by standard cooling theory of irradiated gas giant planets (Fortney et al. 2007).

Ibgui & Burrows (2009) and Ibgui et al. (2011) used a coupled radius–orbit evolutionary model to show that planet radii can be inflated to $2 R_{\rm Jup}$ and beyond during a transient phase of heating caused by tidal circularization of a short ($a \approx 0.1$), highly eccentric ($e \approx 0.8$) orbit. Though, as was noted in both studies, planets can persist in an inflated state for Gyr beyond the circularization of their orbit and the cessation of tidal heating, they do cool and contract significantly prior to full circularization. In each study the orbits are still significantly non-circular ($e \gtrsim 0.1$) when the planets are largest. Thus, under the transient heating scenario, the very largest planets are expected to have a non-zero eccentricity. Though we do measure a non-zero eccentricity for WASP-17b, it is small, and the stringent upper limit that we place on e is inconsistent with current models of one transient phase of tidal heating.

Other than transient heating, ongoing tidal heating may occur if the orbit of a planet were kept non-circular by the continuing interaction with a third body (Ibgui et al. 2010). However, the stringent upper limit we place on e makes this unlikely as the sole cause of the inflation of WASP-17b, as it would necessitate a lower planetary tidal dissipation factor than theoretical models or empirical determinations generally suggest (Ibgui et al. 2010).

If the atmospheric opacity of WASP-17b were enhanced then its internal heat would be lost at a lower rate and contraction would be slowed (Burrows et al. 2007). The atmospheric opacities of WASP-17b may be enhanced if, for example, the strong optical and ultraviolet (UV) irradiation of the planet by its host star produces thick hazes, absorbing clouds and non-equilibrium chemical species (e.g. tholins or polyacetylenes).

The bloated planets are all very strongly irradiated by their host stars, and a small fraction of stellar insolation energy would be

Table 5. System parameters of WASP-17.

Parameter	Symbol	Value	Unit
Orbital period	P	3.7354380 ± 0.0000068	d
Epoch of mid-transit (HJD, UTC)	T_c	$245\,4577.85806 \pm 0.00027$	d
Transit duration	T_{14}	0.1830 ± 0.0017	d
Duration of transit ingress $\approx$ duration of transit egress	$T_{12} \approx T_{34}$	0.0247 ± 0.0017	d
Planet/star area ratio	$(R_{pl}/R_*)^2$	0.01696 ± 0.00026	
Impact parameter	b	$0.401^{+0.059}_{-0.077}$	
Orbital inclination	i	$86.83^{+0.68}_{-0.56}$	$^\circ$
Stellar radial reflex velocity	K_1	53.2 ± 3.4	m s^{-1}
Semimajor axis	a	0.05150 ± 0.00034	au
Centre-of-mass velocity	γ_{rv1}	$-49\,513.67 \pm 0.56$	m s^{-1}
Offset between RV data set rv2 and rv1	$\gamma_{rv2-rv1}$	22.07 ± 0.68	m s^{-1}
Offset between RV data set rv3 and rv1	$\gamma_{rv3-rv1}$	13.5 ± 2.2	m s^{-1}
Offset between RV data set rv4 and rv1	$\gamma_{rv4-rv1}$	25.6 ± 2.8	m s^{-1}
Orbital eccentricity	e	$0.028^{+0.015}_{-0.018}$ $0.0019 < e < 0.0701$ ($3\,\sigma$)	
Expectation value of orbital eccentricity	$\langle e \rangle$	0.0055	
Argument of periastron	ω	$-82.6^{+14.6}_{-2.6}$	$^\circ$
	$e \cos\omega$	$0.00352^{+0.00076}_{-0.00073}$	
	$e \sin\omega$	$-0.027^{+0.019}_{-0.015}$	
Phase of mid-occultation, having accounted for light traveltime	$\phi_{mid-occ.}$	0.50224 ± 0.00050	
Occultation duration	T_{58}	$0.1746^{+0.0056}_{-0.0042}$	d
Duration of occultation ingress $\approx$ duration of occultation egress	$T_{56} \approx T_{78}$	0.0232 ± 0.0016	d
Relative planet–star flux at 4.5 μm	$\Delta F_{4.5\,\mu m}$	0.00229 ± 0.00013	
Relative planet–star flux at 8 μm	$\Delta F_{8\,\mu m}$	0.00237 ± 0.00039	
Planet brightness temperature[a] at 4.5 μm	$T_{b,4.5\,\mu m}$	1881 ± 50	K
Planet brightness temperature[a] at 8 μm	$T_{b,8\,\mu m}$	1580 ± 150	K
Sky-projected stellar rotation velocity	$v \sin I$	$10.05^{+0.88}_{-0.79}$	km s^{-1}
Sky-projected angle between stellar spin and planetary orbit axes	λ	$-148.7^{+7.7}_{-6.7}$	$^\circ$
Star mass	M_*	1.306 ± 0.026	$M_\odot$
Star radius	R_*	1.572 ± 0.056	$R_\odot$
Star density	ρ_*	0.336 ± 0.030	$\rho_\odot$
Star surface gravity	$\log g_*$	4.161 ± 0.026	(cgs)
Star effective temperature	T_{eff}	6650 ± 80	K
Star metallicity	[Fe/H]	-0.19 ± 0.09	
Planet mass	M_{pl}	0.486 ± 0.032	M_{Jup}
Planet radius	R_{pl}	1.991 ± 0.081	R_{Jup}
Planet density	ρ_{pl}	0.0616 ± 0.0080	ρ_{Jup}
Planet surface gravity	$\log g_P$	2.448 ± 0.042	(cgs)
Planet equilibrium temperature[b] (full redistribution)	$T_{P,A=0,f=1}$	1771 ± 35	K
Planet equilibrium temperature[b] (day side redistribution)	$T_{P,A=0,f=2}$	2106 ± 41	K

[a] We modelled both star and planet as blackbodies and took account of only the occultation depth uncertainty, which dominates.
[b] $T_{P,A=0,f} = f^{1/4} T_{eff} \sqrt{R_*/2a}$, where f is the redistribution factor, with $f = 1$ for full redistribution and $f = 2$ for day side redistribution.
We assumed the planet albedo to be zero, $A = 0$.

sufficient to account for the observed degrees of bloating. Guillot & Showman (2002) suggested that the kinetic energy of strong winds, induced in the atmosphere of a short-period planet by the large day–night temperature contrasts that result from tidal locking, may be transported downward and deposited as thermal energy in the deep interior. However, a mechanism to convert the kinetic energy into thermal energy would still be required. Li & Goodman (2010) and Youdin & Mitchell (2010) found that turbulence is efficient at dissipating kinetic energy. Magnetic drag on weakly ionized winds (Perna, Menou & Rauscher 2010) and Ohmic heating (Batygin & Stevenson 2010) are alternative mechanisms.

5.2 Planetary atmosphere

Fortney et al. (2008) hypothesize that the presence of high-opacity TiO and VO gases in the atmospheres of highly irradiated planets (those experiencing an incident flux of $>10^9$ erg s^{-1} cm^{-2}) cause them to have temperature inversions. Thus, with an incident flux of $2.2 \pm 0.2 \times 10^9$ erg s^{-1} cm^{-2}, WASP-17b is expected to have an atmospheric temperature inversion under this hypothesis.

However, Spiegel, Silverio & Burrows (2009) suggest that, for a planet with the insolation level of WASP-17b, it is unlikely that a temperature inversion could be caused by the presence of TiO and VO in the upper atmosphere. They find that a cold trap exists between the hot convection zone and the hot upper atmosphere on the

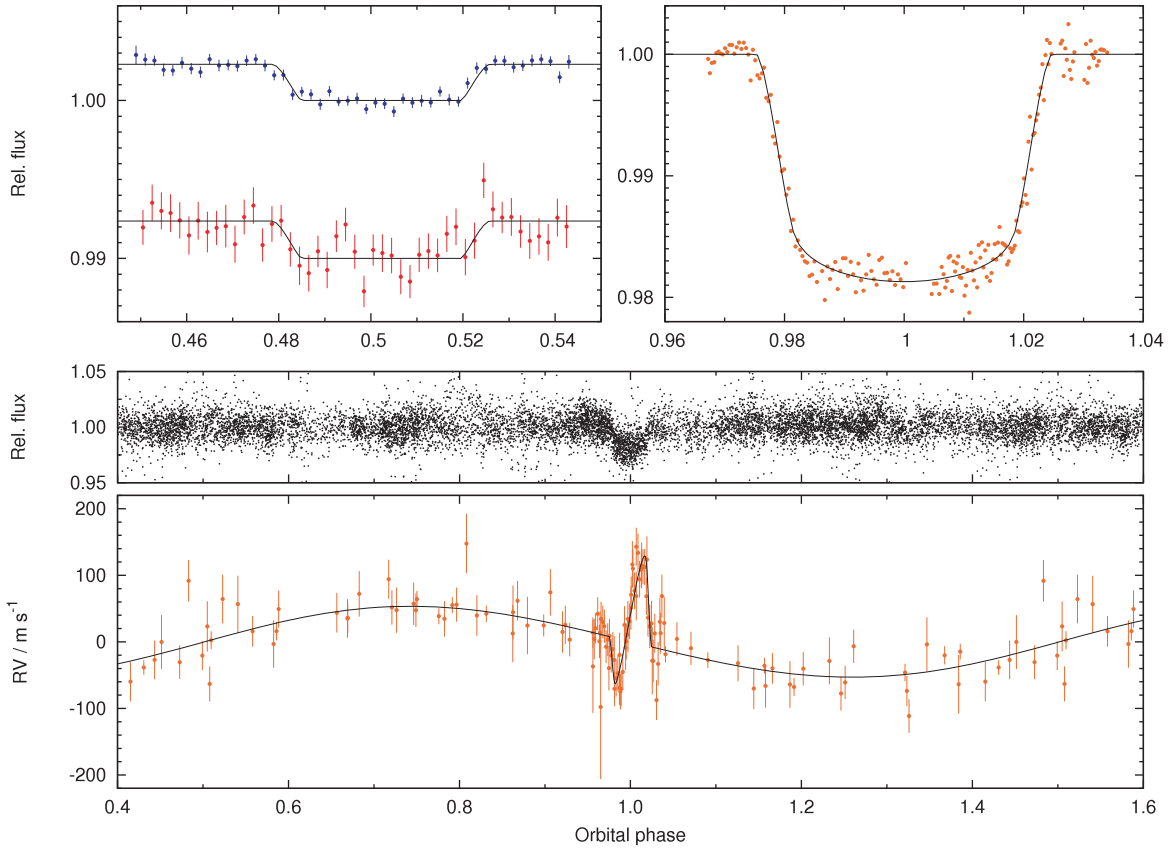

Figure 8. The results of our combined analysis, which combines the new *Spitzer* occultation photometry with existing photometry and RV measurements. The models generated from the best-fitting parameter values of Table 5 are overplotted. Top-left: occultations at 4.5 μm and, offset in relative flux by −0.01, 8 μm. The two occultations per channel from Fig. 1 were binned ($\Delta\phi = 0.002$, ∼11 min) together. Top-right: transit light curve taken with Euler in the I_c band (data from A10). Middle: photometric orbit and transit illustrated by WASP-south data (data from A10). Bottom: spectroscopic orbit and transit illustrated by CORALIE and HARPS data (data from A10 and T10). The measured systemic velocities of each data set (Table 5) have been subtracted.

irradiated day side, in which titanium is likely to form condensates that settle more strongly than does gaseous TiO. Therefore, unless there is extremely vigorous macroscopic mixing and the condensed Ti is lofted back in to the upper atmosphere then it is unlikely that TiO can explain the observed temperature inversions. Not only does VO have the same 'cold trap' issue, but it also has a lower opacity than TiO and is an order of magnitude less abundant.

Knutson, Howard & Isaacson (2010) suggest that planets orbiting chromospherically active stars do not have temperature inversions, and planets orbiting quieter stars do have inversions. They suggest that the high UV flux that planets orbiting active stars are likely to experience destroys the compounds responsible for the observed temperature inversions. Knutson et al. (2010) find the two classes to be delineated by a host-star activity level of $\log(R'_{\rm HK}) \approx -4.9$. Though they caution that the calibration for $\log(R'_{\rm HK})$ is uncertain for stars as hot as WASP-17, they measure the star to be quiet: $\log(R'_{\rm HK}) = -5.3$. WASP-17b is therefore expected to have an atmospheric temperature inversion under this hypothesis as well.

In Fig. 11, the measured 4.5 and 8 μm planet–star flux-density ratios are compared to two model atmosphere spectra of the planet (Barman, Hauschildt & Allard 2005), with parameters taken from Table 5. A blackbody ($T_{\rm P,A\,=\,0} = 1600$ K) is a poor fit to the data and is thus ruled out. In one model atmosphere TiO produces a temperature inversion across the photospheric depths. In the other model, there is no atmospheric TiO. The two models have near-identical 4.5 and 8 μm absolute fluxes, and so we cannot currently discriminate between the two. A precise measurement at 3.6 μm may distinguish between the two cases and thus reveal whether WASP-17b has an atmospheric temperature inversion.

By modelling the planet and star as blackbodies, we used the measured planet–star flux-density ratios to calculate 4.5 and 8 μm brightness temperatures of 1881 ± 50 and 1580 ± 150 K, respectively. We calculate an equilibrium temperature $T_{\rm P,A\,=\,0,f\,=\,1} = 1771 \pm 35$ K by modelling the planet as a blackbody with efficient redistribution of energy from its day side to its night side. The closeness of the brightness temperatures to this equilibrium temperature is consistent with the planet having a low albedo and efficient heat redistribution.

5.3 Misaligned orbit

WASP-17b is in a retrograde orbit. For planet–planet or star–planet scattering to have caused the misalignment between the orbit of WASP-17b and the spin axis of its host star, an additional body must have been present. We looked for evidence of a long-term drift $\dot{\gamma}$ in the RV measurements, which span 716 d, as may be caused by the presence of a long-period companion. From a straight-line fit to the residuals of the radial velocities about the best-fitting model, we get $\dot{\gamma} = -6 \pm 5\,{\rm m\,s^{-1}\,yr^{-1}}$. Hence, there is currently no evidence for a third body in the system, but this does not preclude planet–planet scattering as the cause of the misalignment. Nagasawa et al.

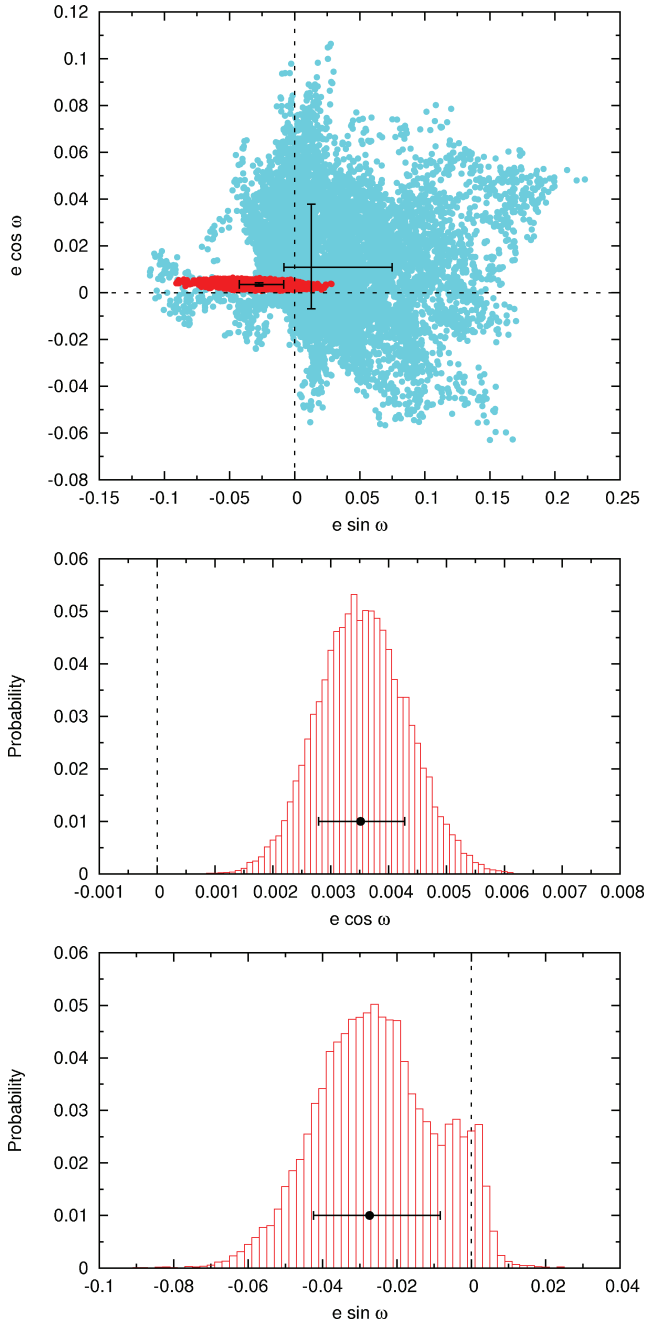

Figure 9. Top panel: a comparison of the posterior probability distributions of $e \cos\omega$ and $e \sin\omega$ from our combined MCMC analysis when including (red dots) and excluding (cyan dots) the occultation photometry. The extent of the error bars show the 1σ confidence limits and their intersections show the median values. Middle panel: normalized histogram of the $e \cos\omega$ posterior probability distribution from our combined MCMC analysis incorporating the *Spitzer* photometry. The point with error bars, arbitrarily placed at probability = 0.01, depicts the best-fitting value and its 1σ error bars. Bottom panel: the same plot as the middle panel, but for $e \sin\omega$.

(2008) found, whilst showing that a combination of planet–planet scattering and the Kozai mechanism can put planets into short, retrograde orbits, that the outer planets can end up at large orbital distances, making them difficult to detect, or they can be ejected from the system.

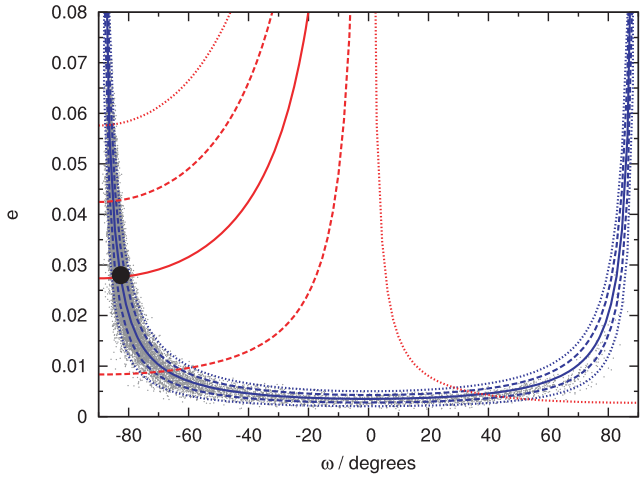

Figure 10. The range of e and ω permitted by the available data. The black dot with error bars shows the best-fitting values from our combined MCMC analysis. The grey dots are the values in accepted MCMC steps. The solid blue and red lines show the values of e and ω that would be indicated by, respectively, the best-fitting values of $e \cos\omega$ and $e \sin\omega$ on their own. The dashed and the dotted lines bound the parameter space permitted by the 1σ and the 2σ limits, respectively, on those parameters, with the same colour scheme applying. Note that, as the 2σ upper limit on $e \sin\omega$ is positive, almost all values of ω are consistent with the data at the 2σ level (providing $e < 0.01$).

5.4 System age

We interpolated the stellar evolution tracks of Marigo et al. (2008) using ρ_* from Table 5 and the values of $T_{\rm eff}$ and [Fe/H] from T10 (Fig. 12). This suggests an age of 2.65 ± 0.25 Gyr and a mass of 1.20 ± 0.05 $M_\odot$ for WASP-17.

Assuming the stellar-spin axis to be in the sky plane, the measured $v \sin I$ of WASP-17 and its derived stellar radius (Table 5) indicate an upper limit to the rotational period of $P_{\rm rot} = 7.91 \pm 0.75$ d. Combining this with the $B - V$ colour of an F6V star from Gray (2008), and the relationship of Barnes (2007), we estimate an upper limit on the gyrochronological age of 1.9 ± 0.5 Gyr. We found no evidence for rotational modulation in the WASP light curves.

We calculated a tidal circularization time-scale of $\tau_{\rm circ} = 5$ Myr for WASP-17b by using the best-fitting values of the planetary ($Q_{\rm P} = 10^{5.5}$) and stellar ($Q_* = 10^{6.5}$) tidal dissipation factors of Jackson, Greenberg & Barnes (2008a) in their equation (1). As the values of the tidal dissipation factor are highly uncertain ($Q_{\rm P} = 10^5$–10^8, $Q_* = 10^5$–10^8; e.g. Ibgui et al. 2011), a range of $\tau_{\rm circ} = 2$–1700 Myr is possible.

With $T_{\rm eff} = 6650 \pm 80$ K (T10), WASP-17 is in the 'lithium gap' (or 'dip'), which is the range of $T_{\rm eff} = 6600 \pm 150$ K in which stars are depleted in lithium by a factor of 30 or more than in hotter and cooler stars (see Balachandran 1995, and references therein). The upper limit placed on the lithium abundance ($A_{\rm Li}$ <1.3) in A10 is consistent with this. Thus, lithium is not an effective indicator of age for WASP-17.

6 CONCLUSIONS

6.1 Science

With a radius of $2.0 R_{\rm Jup}$, WASP-17b is larger than any other known planet by $0.2 R_{\rm Jup}$ and it is $0.7 R_{\rm Jup}$ larger than predicted by standard

Table 6. Effect of occultation light curves on best-fitting orbital eccentricity.

Included occultation photometry	e	ω (°)	$e\cos\omega$	$e\sin\omega$	$T_{\rm occ} - T_{\rm occ,circular}$ (min)[a]
4.5 μm, 2009 April 24	$0.052^{+0.017}_{-0.020}$	$-85.9^{+2.7}_{-1.2}$	$0.00371^{+0.00085}_{-0.00086}$	$-0.051^{+0.020}_{-0.017}$	12.7 ± 2.9
4.5 μm, 2009 May 1	$0.0055^{+0.0075}_{-0.0024}$	-13^{+82}_{-56}	$0.00302^{+0.00103}_{-0.00098}$	$-0.001^{+0.008}_{-0.007}$	$10.3^{+3.5}_{-3.4}$
8 μm, 2009 April 24	$0.015^{+0.059}_{-0.012}$	-92^{+184}_{-21}	$0.0021^{+0.0039}_{-0.0067}$	$-0.005^{+0.011}_{-0.062}$	$-7.3^{+13.2}_{-23.2}$
8 μm, 2009 May 1	$0.049^{+0.020}_{-0.024}$	$-82.2^{+7.1}_{-2.4}$	$0.00662^{+0.00099}_{-0.00111}$	$-0.049^{+0.024}_{-0.020}$	$22.7^{+3.4}_{-3.8}$
None	$0.038^{+0.045}_{-0.026}$	$52.6^{+14.6}_{-2.6}$	$0.011^{+0.027}_{-0.018}$	$0.013^{+0.062}_{-0.021}$	37^{+92}_{-61}
All	$0.028^{+0.015}_{-0.018}$	$-82.6^{+14.6}_{-2.6}$	$0.00352^{+0.00076}_{-0.00073}$	$-0.027^{+0.019}_{-0.015}$	12.0 ± 2.5
All (decon. phot.)	$0.022^{+0.016}_{-0.016}$	$-81.2^{+27.4}_{-3.7}$	$0.00335^{+0.00073}_{-0.00075}$	$-0.022^{+0.017}_{-0.016}$	11.5 ± 2.6

[a] $T_{\rm occ}$ is the time of mid-occultation derived from a simultaneous MCMC analysis.

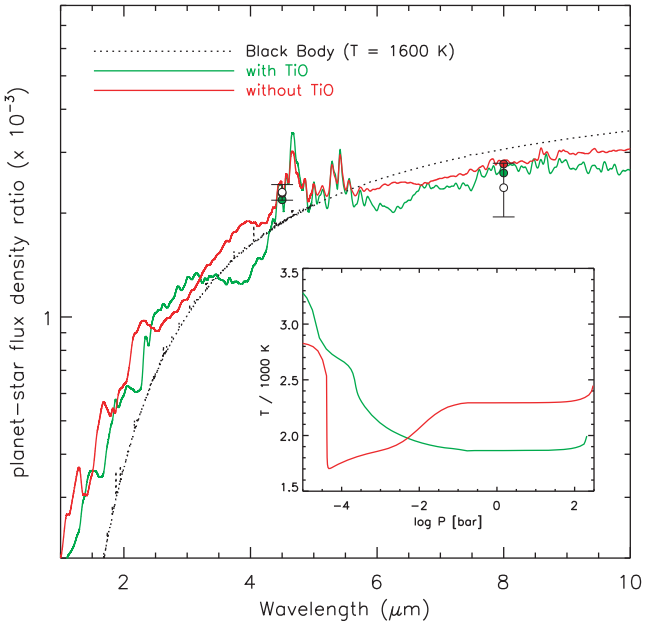

Figure 11. Comparison of planet–star flux density measurements with two model planet atmospheres and with a blackbody. The model atmosphere with TiO exhibits a temperature inversion that extends down to photospheric depths, whilst the model without TiO does not. Inset: temperature–pressure profiles for the two model atmospheres.

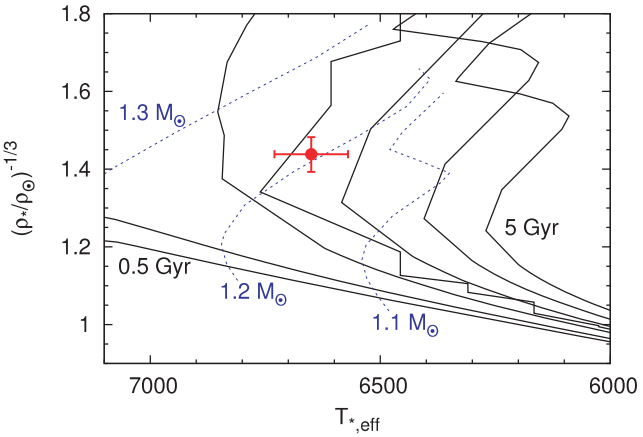

Figure 12. Modified Hertzsprung–Russell (HR) diagram. The isochrones ($Z = 0.012 \approx$ [Fe/H] $= -0.19$) for the ages 0.5, 1, 2, 2.5, 3, 4 and 5 Gyr are from Marigo et al. (2008) and the evolutionary mass tracks ($Z = 0.012 \approx$ [Fe/H] $= -0.019$; $Y = 0.30$) are from Bertelli et al. (2008). To obtain the mass tracks, we performed a simple linear interpolation of their $Z = 0.0008$ and 0.017 tracks.

cooling theory of irradiated gas giant planets. The extent of the planet's inflation is difficult to explain with current models.

Our *Spitzer* occultation photometry gives much tighter constraints on orbital eccentricity than existing RV data alone, thus permitting an accurate determination of the stellar and planetary radii. We have shown that WASP-17b is in a slightly eccentric orbit, with $0.0017 < e < 0.0701$ (3σ). The stringent upper limit we have placed on eccentricity suggests that a transient phase of tidal heating alone could not have inflated the planet to its measured radius. Nor could ongoing tidal heating involving a third body, unless the planetary tidal quality factor is smaller than the best theoretical and empirical determinations.

We find no evidence in the RV measurements for a third body in the system, the presence of which would be necessary to excite the eccentricity of WASP-17b for tidal heating to be ongoing, and may have been necessary to misalign the planet's orbital axis with the spin axis of the star.

Our 4.5 and 8 μm planet–star flux-density ratios do not probe the existence of the expected atmospheric temperature inversion, but a measurement at 3.6 μm may do so. Though the ratios are inconsistent with a blackbody atmosphere, they are consistent with a low-albedo planet that efficiently redistributes heat from its day side to its night side.

6.2 *Spitzer* data

To determine correctly the photometric uncertainties and the optimal aperture radii to use for *Spitzer* data, account must be taken of the counts removed during sky-dark subtraction.

When the background is bright relative to the target at 8 μm, the measured occultation depth can depend sensitively on the choice of aperture radius. In these circumstances detrending with detector position vastly reduces the dependency. An alternative is to perform deconvolution photometry.

In addition to the known hour-long oscillations of *Spitzer*'s pointing about the nominal position, there is also a high-frequency jitter, with periods of 1–2 min. So, when accounting for the inhomogeneous detector response (or 'pixel phase' effect), one should detrend target flux with the unsmoothed target detector positions.

ACKNOWLEDGMENTS

This work is based in part on observations made with the *Spitzer Space Telescope*, which is operated by the Jet Propulsion Laboratory, California Institute of Technology under a contract with

NASA. Support for this work was provided by NASA through an award issued by JPL/Caltech. MG acknowledges support from the Belgian Science Policy Office in the form of a Return Grant.

REFERENCES

Anderson D. R. et al., 2010a, A&A, 513, L3
Anderson D. R. et al., 2010b, ApJ, 709, 159 (A10)
Balachandran S., 1995, ApJ, 446, 203
Barman T. S., 2008, ApJ, 676, L61
Barman T. S., Hauschildt P. H., Allard F., 2005, ApJ, 632, 1132
Barnes S. A., 2007, ApJ, 669, 1167
Batygin K., Stevenson D. J., 2010, ApJ, 714, L238
Bayliss D. D. R., Winn J. N., Mardling R. A., Sackett P. D., 2010, ApJ, 722, L224
Bertelli G., Girardi L., Marigo P., Nasi E., 2008, A&A, 484, 815
Burrows A., Hubeny I., Budaj J., Hubbard W. B., 2007, ApJ, 661, 502
Charbonneau D. et al., 2005, ApJ, 626, 523
Charbonneau D., Knutson H. A., Barman T., Allen L. E., Mayor M., Megeath S. T., Queloz D., Udry S., 2008, ApJ, 686, 1341
Collier Cameron A. et al., 2007, MNRAS, 380, 1230
Enoch B., Collier Cameron A., Parley N. R., Hebb L., 2010, A&A, 516, A33
Fabrycky D., Tremaine S., 2007, ApJ, 669, 1298
Fazio G. G. et al., 2004, ApJS, 154, 10
Ford E. B., 2006, ApJ, 642, 505
Ford E. B., Rasio F. A., 2008, ApJ, 686, 621
Fortney J. J., Marley M. S., Barnes J. W., 2007, ApJ, 659, 1661
Fortney J. J., Lodders K., Marley M. S., Freedman R. S., 2008, ApJ, 678, 1419
Fressin F., Knutson H. A., Charbonneau D., O'Donovan F. T., Burrows A., Deming D., Mandushev G., Spiegel D., 2010, ApJ, 711, 374
Gaudi B. S., Winn J. N., 2007, ApJ, 655, 550
Gillon M., Pont F., Moutou C., Bouchy F., Courbin F., Sohy S., Magain P., 2006, A&A, 459, 249
Gillon M., Magain P., Chantry V., Letawe G., Sohy S., Courbin F., Pont F., Moutou C., 2007, in Afonso C., Weldrake D., Henning T., eds, ASP Conf. Ser. Vol. 366, Transiting Extrapolar Planets Workshop. Astron. Soc. Pac., San Francisco, p. 113
Gray D. F., 2008, The Observation and Analysis of Stellar Photospheres. Cambridge Univ. Press, Cambridge
Guillot T., Showman A. P., 2002, A&A, 385, 156
Harrington J., Luszcz S., Seager S., Deming D., Richardson L. J., 2007, Nat, 447, 691
Howell S. B., 1989, PASP, 101, 616
Ibgui L., Burrows A., 2009, ApJ, 700, 1921
Ibgui L., Burrows A., Spiegel D. S., 2010, ApJ, 713, 751
Ibgui L., Spiegel D. S., Burrows A., 2011, ApJ, 727, 75
Jackson B., Greenberg R., Barnes R., 2008a, ApJ, 678, 1396
Jackson B., Greenberg R., Barnes R., 2008b, ApJ, 681, 1631
Knutson H. A., Charbonneau D., Allen L. E., Burrows A., Megeath S. T., 2008, ApJ, 673, 526
Knutson H. A., Howard A. W., Isaacson H., 2010, ApJ, 720, 1569
Leconte J., Chabrier G., Baraffe I., Levrard B., 2010, A&A, 516, A64
Li J., Goodman J., 2010, ApJ, 725, 1146
Magain P., Courbin F., Sohy S., 1998, ApJ, 494, 472
Magain P., Courbin F., Gillon M., Sohy S., Letawe G., Chantry V., Letawe Y., 2007, A&A, 461, 373
Marigo P., Girardi L., Bressan A., Groenewegen M. A. T., Silva L., Granato G. L., 2008, A&A, 482, 883
Nagasawa M., Ida S., Bessho T., 2008, ApJ, 678, 498
Perna R., Menou K., Rauscher E., 2010, ApJ, 719, 1421
Pollacco D. et al., 2008, MNRAS, 385, 1576
Press W., Flannery B., Teukolsky S., Vetterling W., 1992, Numerical Recipes in C: The Art of Scientific Computing. Cambridge Univ. Press, Cambridge
Reach W. T. et al., 2005, PASP, 117, 978
Schwarz G., 1978, Ann. Statistics, 6, 461
Seager S., Mallén-Ornelas G., 2003, ApJ, 585, 1038
Shannon C., 1949, Proc. IRE, 37, 10
Spiegel D. S., Silverio K., Burrows A., 2009, ApJ, 699, 1487
Swain M. R., Vasisht G., Tinetti G., Bouwman J., Chen P., Yung Y., Deming D., Deroo P., 2009, ApJ, 690, L114
Triaud A. H. M. J. et al., 2010, A&A, 524, A25 (T10)
Werner M. W. et al., 2004, ApJS, 154, 1
Wheatley P. J. et al., 2010, preprint (arXiv:1004.0836)
Youdin A. N., Mitchell J. L., 2010, ApJ, 721, 1113

This paper has been typeset from a TEX/LATEX file prepared by the author.